Received: 10 February 2021 | Revised: 12 April 2021 | Accepted: 10 May 2021

DOI: 10.1111/ijac.13800

International Journal of Applied Ceramic TECHNOLOGY

SPECIAL ISSUE ARTICLE

Electrically conductive silicon oxycarbide thin films prepared from preceramic polymers

Emmanuel III Ricohermoso[1] | Florian Klug[2] | Helmut Schlaak[2] | Ralf Riedel[1] | Emanuel Ionescu[1]

[1]Fachbereich Material- und Geowissenschaften, Technische Universität Darmstadt, Darmstadt, Germany

[2]Fachbereich Elektrotechnik und Informationstechnik, Technische Universität Darmstadt, Darmstadt, Germany

Correspondence
Emmanuel III Ricohermoso, Fachbereich Material- und Geowissenschaften, Technische Universität Darmstadt, Otto-Berndt-Str. 3, D-64287 Darmstadt, Germany.
Email: emmanuel_iii.ricohermoso@tu-darmstadt.de

Funding information
The authors gratefully acknowledge funding from the German Science Foundation (DFG, Germany)—grants no. 411658150 (Microstructured C/SiCX (X = O,N)-based high-temperature strain gauge). Additionally, EI acknowledges funding from DFG within the Heisenberg program (IO 64/14-1).

Abstract

This work focuses on silicon oxycarbide thin film preparation and characterization. The Taguchi method of experimental design was used to optimize the process of film deposition. The prepared ceramic thin films with a thickness of c. 500 nm were characterized concerning their morphology, composition, and electrical properties. The molecular structure of the preceramic polymers used for the preparation of the ceramic thin films as well as the thermomechanical properties of the resulting SiOC significantly influenced the quality of the ceramic films. Thus, an increase in the content of carbon was found beneficial for the preparation of crack-free thin films. The obtained ceramic films exhibited increased electrical conductivity as compared to monolithic SiOC of similar chemical composition. This was shown to correlate with the unique hierarchical microstructure of the SiOC films, which contain large oxygen-depleted particles, mainly consisting of highly graphitized carbon and SiC, homogeneously dispersed in an oxygen-containing amorphous matrix. The matrix was shown to also contain free carbon and to contribute to charge carrier transport between the highly conductive large particles. The ceramic thin films possess electrical conductivities in the range from 5.4 to 8.8 S/cm and may be suitable for implementation in miniaturized piezoresistive strain gauges.

KEYWORDS

electrical conductivity, polymer-derived ceramics, thin film

1 | INTRODUCTION

Over the past six decades, there have been numerous studies reporting on synthesis routes, characterization methods, and the development of new types of polymer-derived ceramics (PDCs).[1,2] Most of the existing studies are intensively done on powders, fibers, and monoliths based on PDCs, while relatively few are conducted on thick and thin film samples. Furthermore, the applicability of PDC for industrial and commercial consumers is getting recognition only in recent years.

Silicon oxycarbide, a type of PDC mostly derived from polysiloxanes, is of interest because of its thermal stability, relatively low process temperature, tunable microstructure, chemical and oxidation resistance, and functional properties which includes electrical conductivity and piezoresistivity.[1,3] Interestingly, the aforementioned properties of

SiOC are dependent on the content of the free carbon phase present in the system. Precursors lead to different microstructures and rearrangements depending on the process temperature. It has been identified that in the SiOC system, the free carbon phase is always the first one to segregate at 500–800°C in the form of polycyclic aromatic hydrocarbons (PAHs). As the heat treatment temperature increases, these aromatics tend to stack up forming carbon-based basic structural units (BSUs) consisting of at least two layers with c. 1 nm lateral extension.[4,5] At 1000–1200°C, hydrogen removal occurs leaving neighboring BSU to form edge-to-edge linkages. This leads to clusters of graphene-like carbon with an increased degree of ordering. Thermal treatment at 1300°C promotes the crystallization of the SiC phase parting the SiO_2 as the matrix of the material.[6] Additional heat treatment above 1700°C results in the ordering of crystallites forming misaligned graphene sheets stacked in a turbostratic manner.[7,8]

Several studies on SiOC ceramics showed conductive behavior having conductivity values ranging from 10^{-3} to 10 S/cm at room temperature conditions.[8–10] Rosenburg et al showed the logarithmic dependence of the SiOC conductivity on the content of segregated carbon of the sample.[10] The dependence showed attribution to the nature of the percolating system which is reliant on the aspect ratio of the free carbon phase.[11] The ordering of the free carbon phase leads to a higher aspect ratio of the conductive phase within the system thus decreasing the percolation threshold. While these data are available for bulk samples, reports for SiOC films are still scarce.

The present work is dedicated to promoting the knowledge transfer of monolithic SiOC to thin film materials to be integrated into microelectromechanical systems (MEMS), for example, as miniaturized SiOC-based strain sensor elements. Specific to this study is producing the base functional material as a homogenous SiOC film on a silicon wafer substrate. The SiOC films are extensively characterized concerning their morphology and microstructure, composition, and electrical properties. As part of the main challenge, this work emphasizes the production of thin films without using filler materials and is done in a single-layer deposition technique. Additionally, the technique must be simple and reproducible and will be analyzed statistically to evaluate the microstructural and electrical properties of the thin film.

2 | MATERIALS AND METHODS

2.1 | Materials

Commercially available Polyramic® SPR 212 (Starfire Systems Ltd.), and BELSIL® PMS-MK (Wacker Chemie AG) were used as polymer precursors for the synthesis of SiOC thin films. To improve the polymerization process, catalysts were used namely 1 wt% of dicumyl peroxide (added as a 50 wt% solution in toluene) and 1 wt% zirconium acetylacetonate for SPR 212 and MK PMS, respectively. Toluene was also added to obtain a 40% dilution of the polymers prior to the spin coating deposition on circular boron-doped p-type Si (100) substrates with 525 μm thickness (Prime Si + SiO_2, MicroChemicals GmbH). The used substrates have a SiO_2 passivation layer with a thickness of 500 nm.

2.2 | Coating preparation

The spin coating process was carried out using LabSpin 8 (Süss MicroTec SE) with a static dispense technique. The substrate was firstly cleaned with acetone and isopropanol before carrying out the process as designed in Table S2. The process was optimized using three parameters namely the initial spin speed, the acceleration profile, and the final spin speed. All three parameters were identified to influence the thickness and uniformity of the film. The design of the experiment (DOE) presented in Table S2 utilized the L9 (33) Taguchi static design which reduced the number of trials to 9 instead of 27 of the full factorial design.[12–14] The film thickness was chosen as the response factor which was measured using a profilometer (Dektak XT Advanced System, Brucker), in three different positions. The final set of parameters used in the experiments is listed in Table S1.

The samples were then thermally cross-linked at 250°C in air. After cross-linking, the sample was pyrolyzed in a graphite crucible placed in a high-temperature furnace (FCT-Uniaxial hot-press, FCT Systeme GmbH). The temperature was first ramped up to 1100°C then held for 2 h. It was then ramped up to 1400°C for an additional heat treatment step which was then held for 3 h. The whole heat treatment process used constant heating and cooling rates at 5°C/min and was all done under a high purity nitrogen atmosphere.

2.3 | Coating characterization

The coatings were analyzed using a profilometer, an in-house four-probe resistance measurement device, Raman Spectroscopy (LabRAM Horiba HR Raman Spectroscope HR800, Horiba Jobin Yvon GmbH), Scanning Electron Microscopy [SEM] coupled with Energy Dispersive Spectroscopy [EDS] (JEOL JSM 7600F, JEOL Ltd.), and Conductive-[C-AFM], and Tunneling Atomic Force Microscopy [TUNA] (Bruker Dimension Icon, Bruker) with AC240 TM conductive tip (Oxford Instruments).

3 | RESULTS AND DISCUSSION

3.1 | Thin film deposition optimization

According to the review article of Barroso et al, a critical coating thickness of several μm (up to 10 μm) must be considered when dealing with PDCs for thin film application, to prevent cracking and spallation.[15] For instance, the work of Günthner and Kraus showed that a filler-free PDC-based coating has a critical coating thickness of 1 μm which is in agreement with the preliminary experiments of this study.[16,17] For thicker PDC-based coatings, the use of suitable fillers is required to compensate for the formation of cracks during shrinkage of the film.[15]

Conducive to these findings, the envisaged film thickness for the SiOC films prepared in the present study was kept below 1 μm to partake a crack-free SiOC coating on a silicon substrate. The spin coating process has been used in a wide variety of industries and technology sectors for silicon wafer coatings due to its simplicity, readiness, and high reproducibility. The use of the spin coating process in nanotechnology has been prevalent especially for semiconductor applications that require thin films with high uniformity. The thickness of the film depends on several factors such as rotational forces, precursor viscosity, and the adhesion of the solution with the substrate.[18,19] In the present study, the process-related factors namely the initial and secondary spin speed, as well as the acceleration was identified as the control factors while the deviations in solution concentration, working environment conditions, and user effect were considered being the noise factors.

To analyze the effect of the three factors identified in Table S2, the Taguchi method is utilized. The Taguchi method was championed by Genichi Taguchi in 1987 and is a powerful approach to optimize the experimental design performance. This method determines the robustness of the design by taking the prime permutation of design parameters from a minimum number of experiments hence ensuring the reproducibility of the results. In this experiment, results are obtained by performing 9 trials instead of 27 rivaled to a full factorial design of the experiment.

As shown in Table S3, analysis of variance (ANOVA) done at 95% confidence level revealed the initial spin speed as the main control factor responsible for the film thickness uniformity with a p-value of 0.027, F-statistic (df = 2) of 36.64. Given that the p-values of the second spin speed and the acceleration were both more than the alpha = 0.05, the null hypothesis was accepted stating the insignificance of both factors to the thickness homogeneity. Although statistically insignificant, it is imperative to look at the practical aspect of the experiment. Considering Figure 1, the significance of using the high initial spin speed has been highlighted by the decreasing number of cracks seen on the surface of the film, however, some cracks are still present on the sample

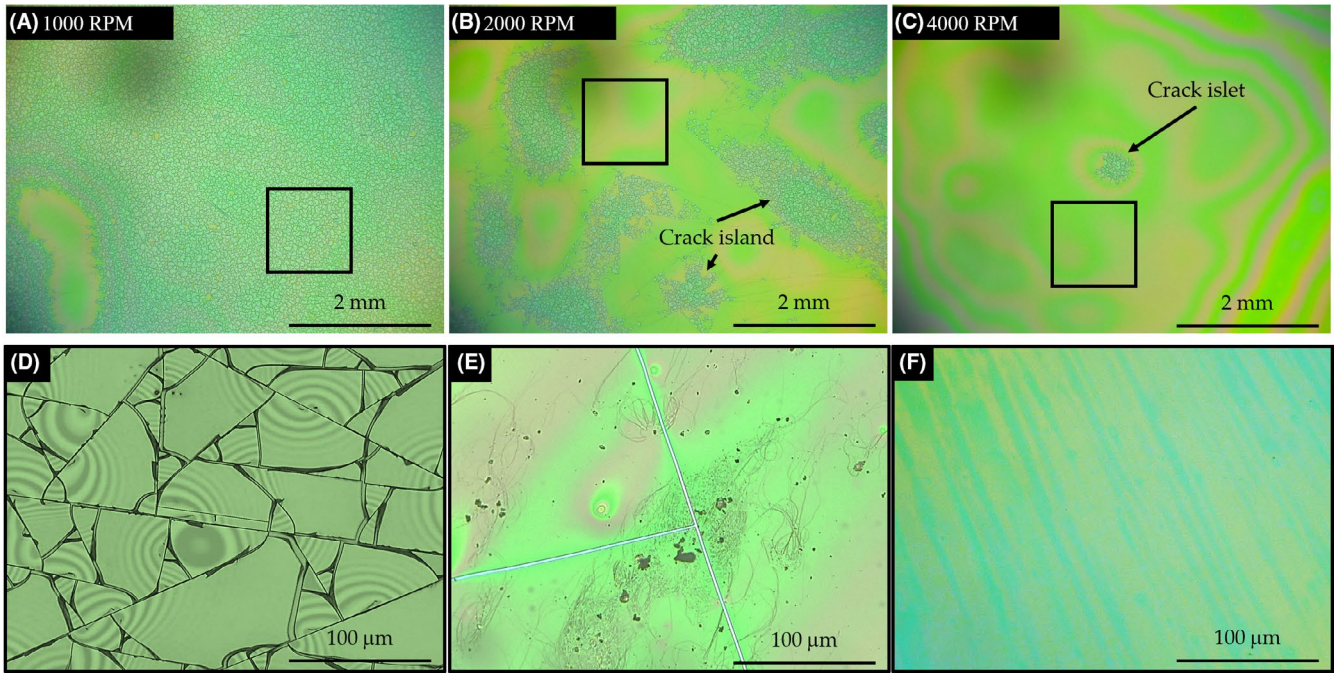

FIGURE 1 Optical microscopic images of the thin Si-polymer film derived from SPR 212 after crosslinking at 250°C. Samples were spin coated at different initial spin speeds with the acceleration of 300 rpm per second, and a second spin speed of 6000 rpm. (A) At the initial spin speed of 1000 rpm, almost the whole surface is crammed with micro-cracks. (B) Crack islands can be seen on the surface of samples spin coated at an initial speed of 2000 rpm which then decreased as the spin speed was changed to (C) 4000 rpm. (D–F) Magnified areas of images (A–C) highlighting the quality of the film surface

spun at 4000 rpm. These cracks are then eliminated when the effect of the second spin speed at 8000 rpm is taken into consideration. The film thickness measured with this set of the parameter is approximately 500 nm after the final heat treatment process.

The Taguchi method considers the means and the signal-to-noise (S/N) ratio of the results to reduce the variability of the design. The S/N ratio is the response tradeoff when setting the mean value to the desired level while keeping the variance low.[12,14,20] The S/N ratios are defined so that a maximum value of the ratio minimizes variability transmitted from the noise variables.[12] In Figure 2A, it can be seen that most of the runs resulted in mean values close to or above the target thickness of less than 1 μm. Considering these values, the S/N ratio of the results was calculated to minimize the response or using the "smaller-is-better" $(S/N)_S$ type. The desired factors resulted in an initial spin speed of 4000 rpm for 30 s then accelerated to a second spin speed of 8000 rpm for 30 s with an acceleration of 500 rpm/s as shown in Figure 2B.

Following the optimized spin coating parameters, eight supplementary samples were prepared to confirm the effectiveness of the design to which none of the samples manifested crack formation after thermal treatment and ceramization. The samples were cross-linked at 250°C and subsequently pyrolyzed at 1100 and 1400°C, respectively, as the last ceramization step. The samples prepared from Polyramic SPR 212 provided a SiOC material containing c. 17 vol% free carbon (C17-1100 and C17-1400) and produced a homogeneous and crack-free film after heat treatment, as shown in Figures 3C,D and 4. The SEM image of the C17-1100 sample exhibits a smooth surface while phase separation is evident for the C17-1400 sample as supported by the color contrast shown in the backscattered SEM image in Figure 4.

Additionally, samples are prepared from Belsil PMS-MK, a precursor that delivers a SiOC ceramic containing c. 11 vol% free carbon (i.e., C11-1100 and C11-1400). However, SEM images of C11-1100, which are shown in Figure 3A,B, indicated micro-crack formation and spallation. The samples annealed at 1400°C, C11-1400 (not shown), exhibited complete

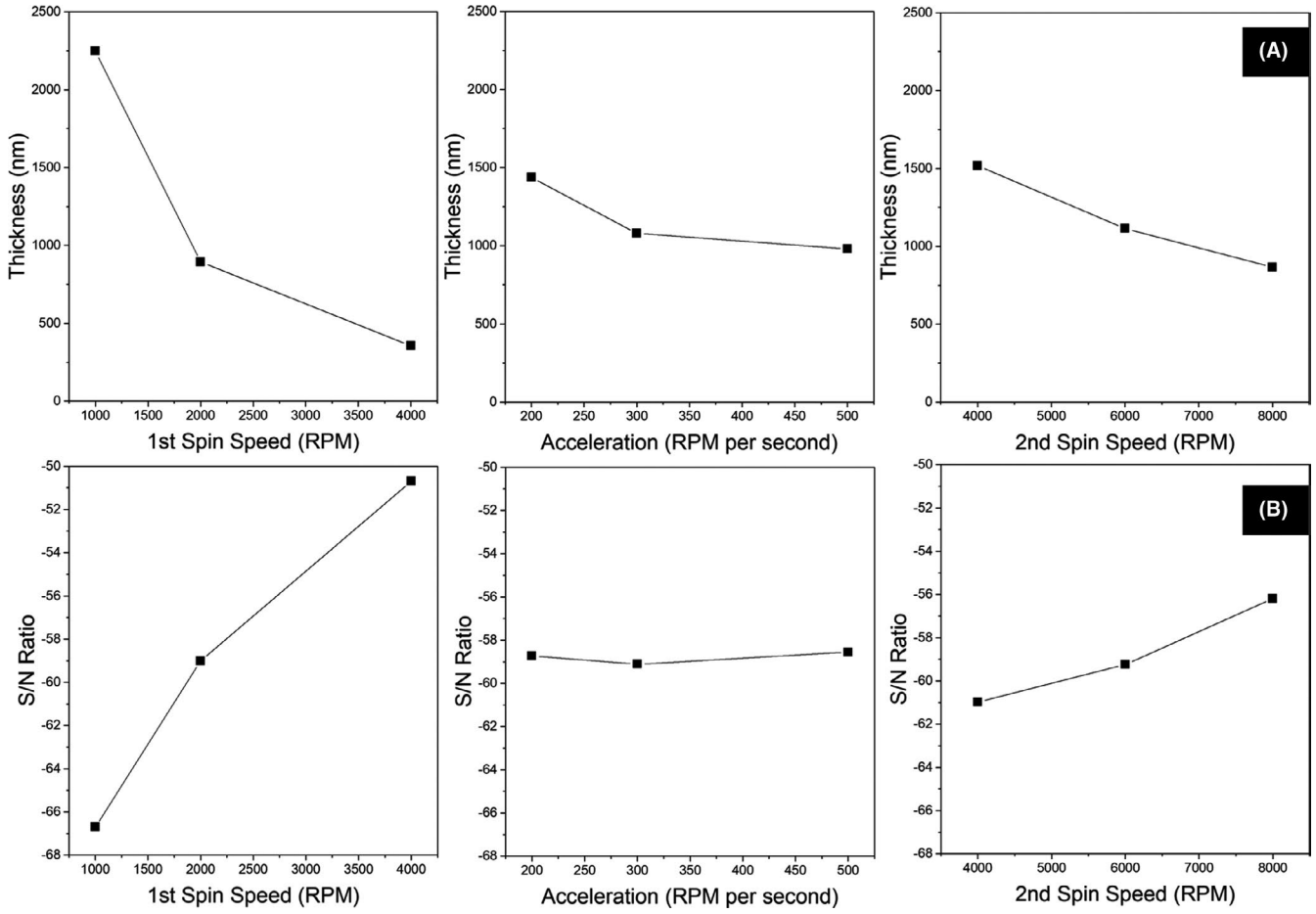

FIGURE 2 Statistical analysis of spin coating process optimization. (A) Main effect analysis of the average thickness obtained after crosslinking. (B) Main effect analysis of the S/N ratio of film thickness as a response to different factors with maximum S/N ratio as the desired outcome. Taguchi design analysis resulted in 4000 rpm, and 8000 rpm as the optimal spin speeds with 500 rpm per second as the acceleration. First spin speed showed to have the most significance in the spin coating process of the preceramic polymer

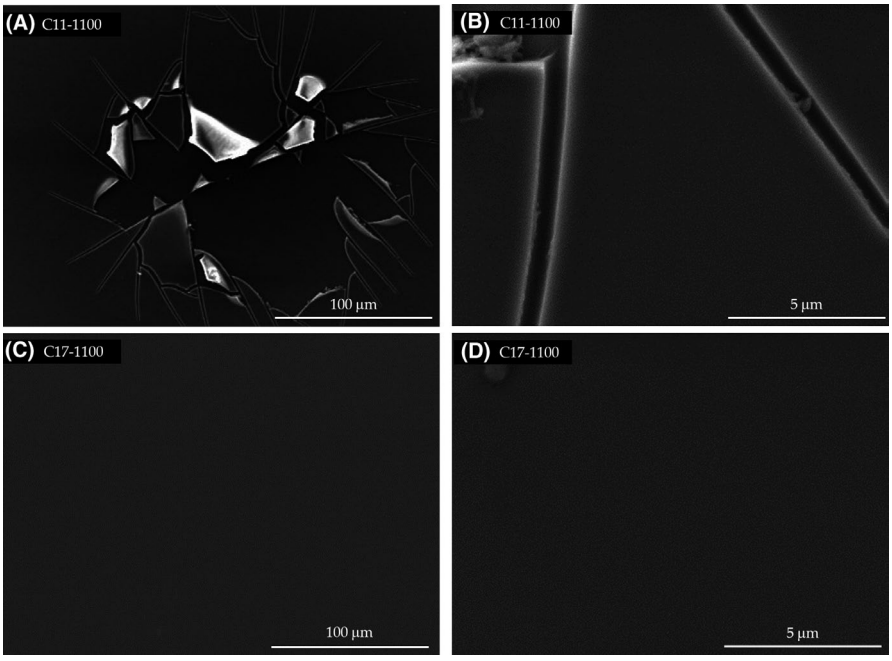

FIGURE 3 SEM images of spin-coated samples after heat treatment at 1100°C. (A and B) Formation of microcracks and spallation on C11-1100 sample. (A) Homogenous coating of sample C17-1100

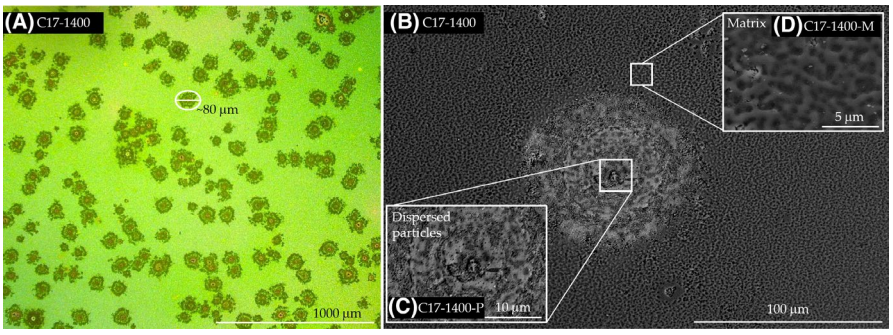

FIGURE 4 Phase separation was observed on the C17 sample heat treated at 1400°C. (A) Optical microscopic image of the C17-1400 film showing the presence of dispersed particles with ~90 µm in size. (B) Backscattered SEM image displaying the color contrast (topographical difference) of the dispersed particle from the matrix of the C17-1400 sample. (C) Magnified image of the precipitate, and (D) magnified image of the matrix

delamination of the film after the heat treatment process. As the preparation parameters for both samples C11 and C17 compositions were kept the same, it is obvious that the use of different preceramic polymers (i.e., SPR-212 vs. PMS-MK) leads to large differences in film quality/integrity besides different composition of the resulting SiOC ceramic films.

In previous studies related to the gel-to-ceramic conversion (e.g., 21–23), it was mentioned that sol–gel films undergo significant structural changes and subsequently suffer from mechanical stresses developed during their thermal treatment, namely heating up, isothermal heat treatment (annealing), and cooling down. These three steps lead to intrinsic and thermal stresses on the thermally treated sol–gel films. Intrinsic stress is experienced by the film during the heating up and annealing steps, during which densification occurs accompanied by chemical and structural changes. In addition, the difference between the coefficients of thermal expansion (α) of the film and the substrate during cooling down gives rise to thermal stress. The TGA results of the preceramic polymers used in this study showed three weight loss steps during their pyrolysis at 1100°C, with onset temperatures at 210, 520, and 700°C, respectively.[24,25] No further weight loss was analyzed in both studied ceramic systems, indicating that the ceramization process is completed at temperatures as high as 700–800°C. Consequently, it is considered that up to temperatures ranging between 700 and 800°C, densification occurs and generating in-plane tensile stress in the films. For thin films, stresses are mainly concentrated on the biaxial direction since shrinkage is not restricted in the direction perpendicular to the substrate.[26] As the film is constrained in two dimensions (i.e., in the plane of the substrate), the tensile stress experienced by the film may cause bending of the substrate or/and indeed cracking of the ceramic film.[15,22,27]

The values of the thermal expansion coefficients and the Poisson's ratio of the SiOC samples and the silicon substrate are presented in Table 1. After cooling, the residual stress

on the film, σ_f, as well as the radius of curvature (R) of the coated substrate was calculated using Equations (1 and 2), respectively, and are presented in Table 1.

In Equation (1), ΔT is the difference between the heat treatment temperature and the room temperature, and $\Delta\alpha$ is the difference between the thermal expansion coefficients of the silicon substrate and the SiOC thin film. The term $\left[\frac{E_f}{1-\nu_f}\right]$ or E^* is the effective stiffness or the biaxial modulus of the film raised by the Poisson effect.[30] Equation (2) was derived from Stoney's equation where E, t, and ν are Young's modulus, thickness, and Poisson's ratio of the silicon substrate, respectively.[27,31]

$$\sigma_f = \left[\frac{E_f}{1-\nu_f}\right] \Delta T * \Delta\alpha \tag{1}$$

$$R = \left[\frac{1}{6 * \sigma_f * t_f}\right] * \left[\frac{E_{Si} * t_{Si}^2}{1-\nu_{Si}}\right] \tag{2}$$

It can be seen from the values of the residual stresses in Table 1 that upon cooling, sample C11 was under tension while sample C17 was under compression. Based on Equation (1) and Table 1, for both samples, the first two terms (E^* and ΔT) of the equation are similar, thus the difference of the residual stresses is mainly caused by the mismatch of the thermal coefficients ($\Delta\alpha$) of the film and the substrate. Given that the thickness of the silicon substrate is much larger than that of the film (t_{Si} (500 μm) >> t_f (500 nm)), the film is forced to follow the dimension of the substrate as reinforced by the calculated radius of curvatures. The positive values of R indicate the concave warpage of the substrate resulting in tensile stress on the film.[32]

As a result, the C11 samples showed the formation of cracks and complete delamination of the film, therefore not meeting the criteria for a uniform and homogenous thin film compatible for MEMS applications. Consequently, the following sections will deal with the study of the samples with 17 vol% C, that is, C17-1100 and C17-1400.

3.2 | Thin film composition

Former studies showed that pyrolysis of the SiOC matrix at 1200°C generally promotes phase separation into SiO_2 and SiC. It has been shown also that with supplementary heat treatment of the sample, SiC can further crystallize as a product of the carbothermal reduction of the SiO_2 phase at a temperature above 1400°C.[9,33,34] These phenomena found in the SiOC system are explained by the Reactions (3) and (4).

$$SiOC \rightarrow SiO_2 + SiC + C, \tag{3}$$

$$SiO_2 + 3C \rightarrow SiC + 2CO \tag{4}$$

The backscattered electron image presented in Figure 5 displays two distinct phases on the surface of C17-1400, with different morphologies. The first phase consists of round-shaped structures evenly distributed (Figure 4A) within the second phase acting as the matrix. SEM images taken at higher magnification revealed that the disperse phase has a porous structure with a sponge-like morphology. The phases were differentiated by their amounts of carbon and oxygen. Thus, the dispersed phase is C-rich and O-depleted; whereas the matrix is O-rich (Figure 5). Therefore, it is assumed that the matrix consists of amorphous, sp^2-hybridized carbon-containing SiOC (C/SiOC); whereas the dispersed phase most probably contains sp^2-hybridized carbon and SiC (C/SiC). The formed SiC usually segregates in form of nanometer-sized crystallites in bulk SiOC while the resulting SiC phase in the SiOC film appears as micrometer-sized particles. In relation to Figure 4A, by particle count distribution, these dispersed particles took up ~16 vol% of the surface of a representative 1 × 1 cm^2 sample size. This value is comparable to the known volume fraction of carbon in the preceramic polymer amounting to 17 vol% with the deviation accounted to the amount of carbon identified in the matrix as per the EDS map shown in Figure 5.

To confirm the presence of sp^2-hybridized C in the thin film samples, Raman spectra of the samples were taken and the results are presented in Figure 6. It can be seen that both samples pyrolyzed at 1100°C have broader peaks and high-intensity values as compared to that of the C17-1400 sample. The matrix and the dispersed particles were analyzed separately and the

TABLE 1 Poisson's ratios (ν (1100°C), ν (1400°C)), and coefficient of thermal expansion (α) values of the SiOC samples, and the silicon substrate.[28,29] Calculated residual thermal stresses on the film (σf-1100, σf-1400) and the calculated curvatures of the coated substrate (R1100, R1400)

Sample	α (10^{-6} K^{-1})	ν (1100°C)	ν (1400°C)	E (GPa)	σf−1100 (MPa)	σf−1400 (MPa)	R_{1100} (mm)	R_{1400} (mm)
C11	2.02	0.11	0.17	90	52.1	71.6	0.26	0.19
C17	3.23	0.11	0.17	90	−79.3	−108.8	−0.17	−0.12
Si	2.5	0.22	-	125	-	-	-	-

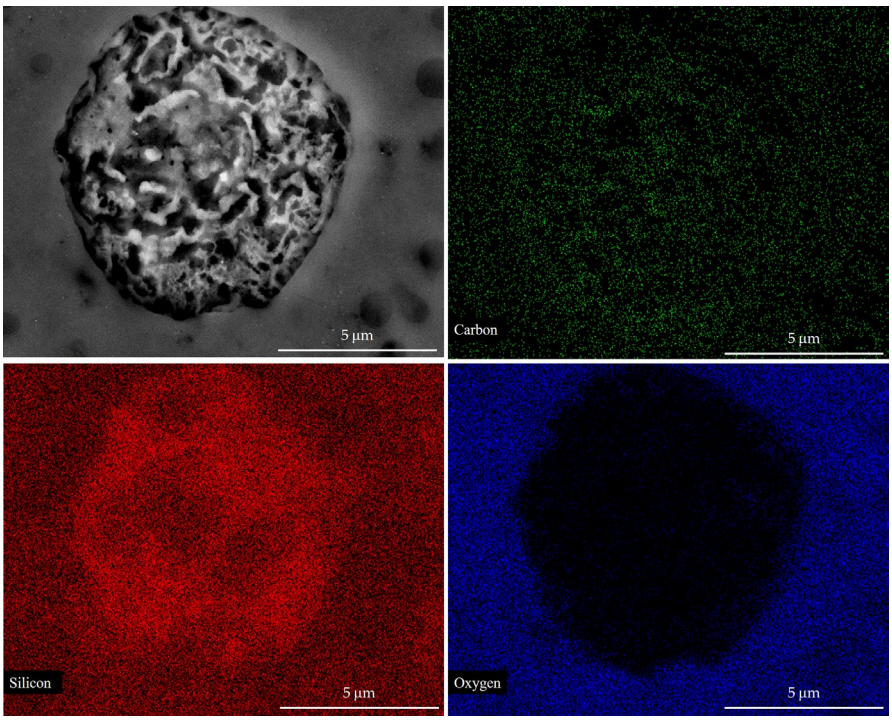

FIGURE 5 Backscattered SEM image and EDS map of C17-1400 thin film: two phases were observed on the film surface. The SEM image reveals a porous structure of the disperse phase

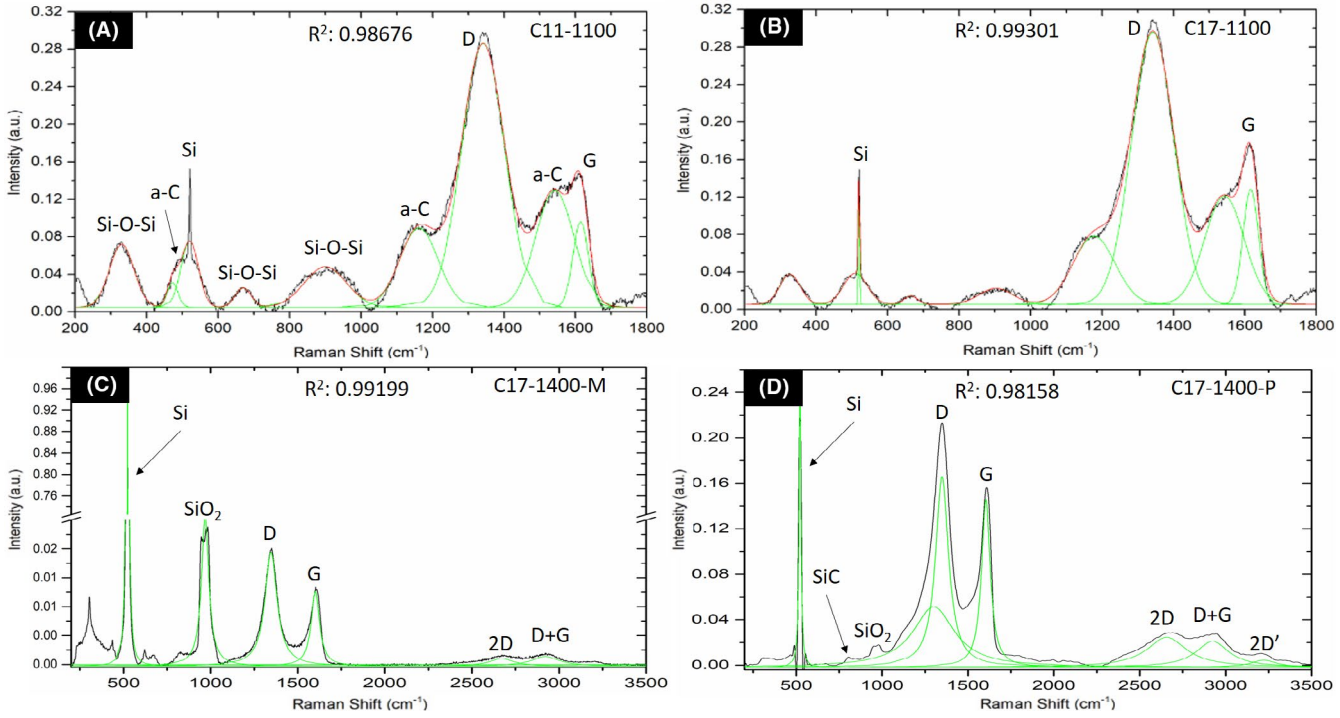

FIGURE 6 Raman spectra of SiOC-based thin film samples. Samples synthesized at 1100°C (i.e., C11-1100 and C17-1100) are shown in (A) and (B), respectively. Spectra in (C) and (D) represent the matrix and C-rich precipitates, respectively, in C17-1400

spectra are presented in Figure 6C,D. Three dominant peaks are found one associated with Si, and the D and G bands of the free carbon phase present in the system.

Having a closer look at the fingerprint area of the Raman spectra depicted in Figure 6, six other peaks are analyzed in the sample obtained at 1100°C which partially or fully disappeared in the sample annealed at 1400°C. In addition to a sharp band at c. 521 cm^{-1}, which was assigned to crystalline Si, silicon substrate-related bands (more precisely, bands related to the silica scale present on the silicon substrate) are

located at 330 and 670 cm^{-1} which are both attributed to the asymmetric and symmetric Si-O-Si vibrations while the peak at 950 cm^{-1} is due to the second-order transverse optic phonon of the silica scale.[35–40] A broad peak at 500 cm^{-1} can also be seen on the samples pyrolyzed at 1100°C which is attributed to the presence of amorphous sp^3 bonded carbon.[41] A peak at 1150 cm^{-1} has been matched with the amorphous carbon phases (a-C) which are related to the used precursor and were found to resemble the theoretical phonon density of states of sp^3 domains.[42–46] A conclusion has been drawn by Chu et al that peak shifts and widening are related to the number of sp^3 and sp^2 neighbors which varies locally. It is further discussed that the peak at 1150 cm^{-1} disappears with decreasing amount of sp^3 carbon atoms.[47]

The shoulder of the Raman peak at 1500 cm^{-1} is also credited to the presence of amorphous carbon (a-C). It is known that the graphitization rate increases with an increasing amount of carbon. Roth et al reported that the disappearance of the a-C peak at higher temperatures indicates the completion of the graphitization process forming nanocrystalline graphitic domains.[48] In this work, amorphous carbon (a-C) fully disappeared after heat treatment at 1600°C which we could not achieve in our present work due to the limitation of the heat treatment temperature related to the melting temperature of the silicon substrate at 1414°C. Looking at the predominant peaks presented in Figure 6, the intensities of the silica-scale related bands for the 1100°C-treated samples are less than those of the 1400°C sample, with the highest relative intensity found in its matrix; this is correlated with the fact that the thickness of the ceramic film decreases as the thermal treatment temperature increases from 1100 to 1400°C. As explained in Section 3A, the film is generally under biaxial stress and is free to move in the z-direction, thus a temperature dependence of the thickness of the film has to be considered. It can be seen that a larger thickness of the film in C11-1100 and C17-1100 results in less intensity of the substrate-related signals (i.e., Si signal at 520 cm^{-1}) as compared to the analogous samples thermally treated at 1400°C. On the other hand, the matrix of the C17-1400 sample has a more intense Si peak as compared to that of the dispersed particles. Additionally, the SiO_2 peak is also more visible in the matrix than that of the dispersed particle area. This finding suggests a thinner structure of the matrix relative to the dispersed particles of the C17-1400 sample and agrees well with the contrast observed in the SEM micrographs (see Figure 5B). The SiC band at 801 cm^{-1} is found in the dispersed particle in the Raman spectrum of the sample C17-1400, which supports the C-rich nature of the segregated particles as already analyzed via EDS mapping shown in Figure 5.

After performing Lorentzian fitting of the Raman spectra presented in Figure 6, first- and second-order features for the sp^2-hybridized free carbon phase were identified in the SiOC thin film. The corresponding values of the Raman line characteristics are listed in Table 2. The presence of the D (disorder) and the G (graphitic) bands of the Raman spectra confirms the formation of segregated carbon phases in samples.[48–50] Both of these bands were acknowledged to have originated from sp^2 hybridized carbon.[42] The D band is the defect-induced double resonance process that activates at the transverse optical (TO) phonon and is often referred to as the disorder band originating with the out-of-plane vibrational mode of graphene at the A_{1g} zone edges. The disorder in the sp^2-hybridized carbon systems results in a resonance of the Raman spectra. The optical phonon dispersion in graphitic material is classified based on the direction of the nearest C-C atoms. The in-plane modes known as transverse (TO) and longitudinal (LO) refer to vibrations perpendicular and

TABLE 2 Mean values of the Lorentzian fitting of the Raman spectra of the SiOC thin film samples as compared to monolithic samples

		Thin film				Monolith			
		C11-1100	C17-1100	C17-1400 M	C17-1400 P	C11-1200	C11-1400	C17-1200	C17-1400
D	Raman Shift	1341.5	1342.3	1346.8	1348.3	1347.9	1362.9	1340.8	1350.8
	FWHM	142.5	139.6	83.6	88.9	97.0	65.5	143.8	97.7
G	Raman Shift	1614.5	1616.1	1601.4	1606.5	1595.0	1597.7	1588.8	1606.2
	FWHM	51.3	51.6	54.5	62.7	66.0	75.9	74.8	60.1
2D	Raman Shift	-	-	2675.7	2656.3	-	-	2611.9	2626.2
	FWHM	-	-	133.9	306.2	-	-	74.8	60.1
Calculations	A_D/A_G	8.6	6.4	2.3	1.4	2.3	1.9	2.8	2.0
	L_a [nm]	2.0	2.6	7.2	11.9	7.3	8.9	6.0	8.3
	L_D [nm]	3.9	4.6	7.5	9.7	7.6	8.4	6.9	8.1
	n_D ($\times 10^{11}$) [cm^{-3}]	29	22	8.0	5.0	7.9	6.4	9.5	6.9
	L_{eq} [nm]	-	-	7.1	56.3	-	-	21.6	23.5

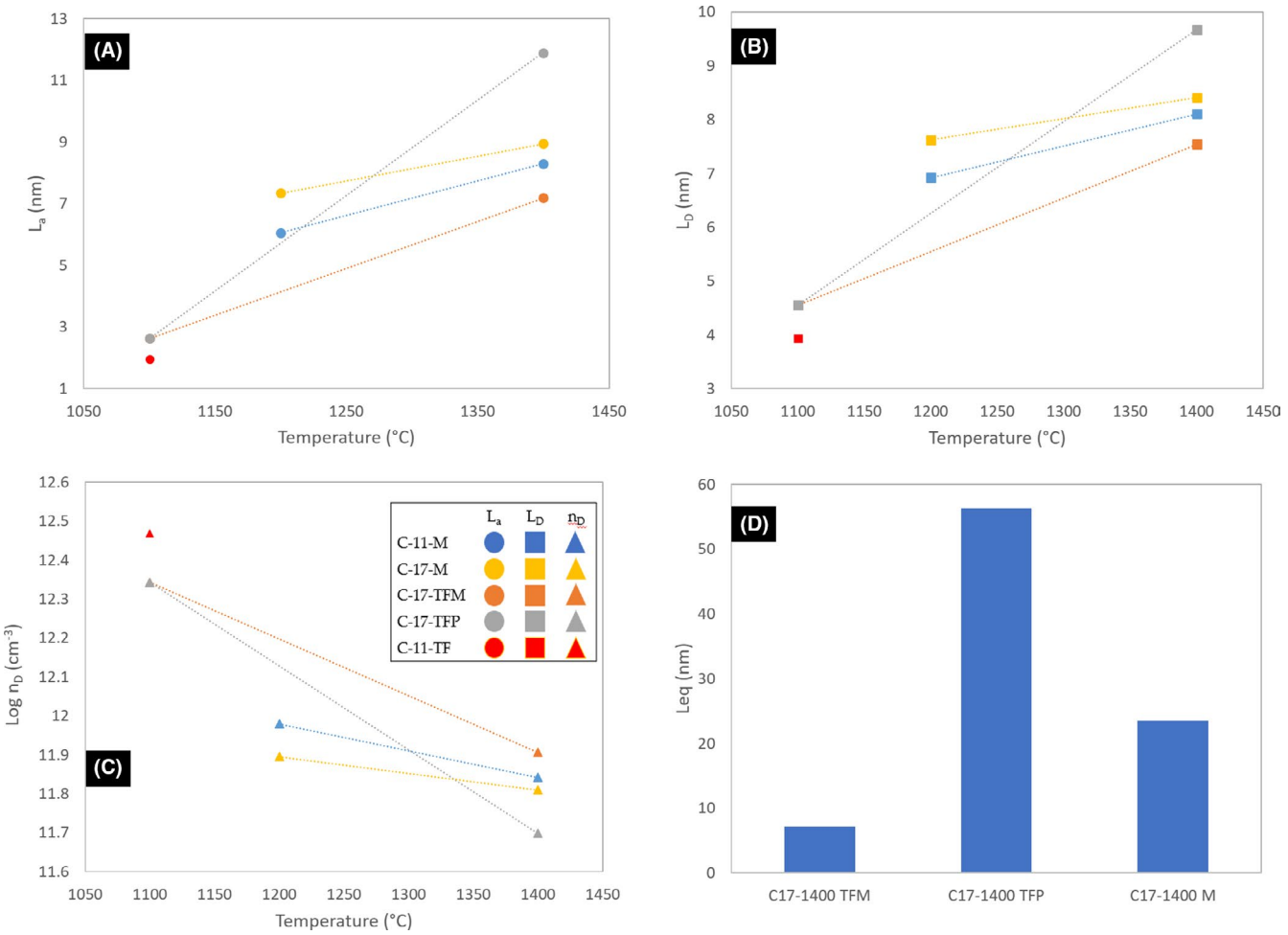

FIGURE 7 Calculated (A) lateral crystal size (L_a), (B) average defect distance (L_D), (C) defect density (n_D), and (D) tortuosity of sp^2 domains of the thin film samples as compared to the work of Rosenburg on SiOC monoliths. Samples are named after the system (C-[vol%C Content]-[M (monolith), TFM (thin film Matrix, TFP (thin film particle)]

parallel to the C-C directions, respectively. On the other hand, the G band is a result of the first-order scattering of the zone-center E_{2g} optical mode of the sp^2 domains primarily caused by in-plane vibrations of carbon atoms.[42,47,51,52] The 2D band, also known as G' band, at 2675 cm^{-1}, is due to the second-order Raman scattering of the in-plane TO phonons near the Brillouin zone.[52–55]

It can be seen that in total, the main bands of the films are blue shifted as compared to pristine graphite with a known G-band located at 1580 cm^{-1}. Three reasons were classified to explain the observed shift of the D and G band peaks of the samples; (1) thermal shift due to the effect of annealing temperature which, however, causes a redshift, (2) due to the increase in sp^3 C amount which results in a blue shift, and (3) due to the effect of the substrate.[8,39,47,51,56–62] For all the thin film samples, it can be seen that the G peak is overlapping with the literature-known position of the D' peak, a double resonance process similar to the D band but occurs at the LO phonon.[55,63,64] The superposition of the G and D' peaks is commonly observed for defective graphenes with a D' shifting to 1580 cm^{-1} for higher defect density.[64] Given the overlap between the two peaks, differentiation between the D' from the G peak can better be done by looking at the presence of the second-order 2D' peak at 3200 cm^{-1} which is also detected here. In the succeeding calculations, the peak at 1610 cm^{-1} is assigned to the G band influenced by the D' band with a high defect contribution. The work of Rosenburg et al demonstrates the temperature dependence of the G-peak position for SiOC samples.[8] Accordingly, the thermal shift is accounted for by the anharmonicity of the in-plane angular modes that are activated as the movement of the atoms directly relates to the increase in temperature. This effect is more pronounced on the optical branches of graphene on its transverse and longitudinal atomic motions.[56,57] As the measurement is conducted at room temperature only, the effect of thermal shifts for SiOC films is hard to notice as compared to the effect of the sp^3 C fraction. This effect has been demonstrated in the work of Merkulov *et al* for samples with 6–75 at.% sp^3 C.[65] Due to the resonant character of the D and G peaks, excitation at the visible range causes the blue shift

which saturates at 1600 cm^{-1}. Lastly, it has been reported that Si/SiO_2 substrate generally causes the shift of the G band up to 12 cm^{-1} which can be attributed to the effect of unintentional doping of the film caused by the charge impurities present on the substrate.[60–62]

The ratio of the intensities of the D and G bands (I_D/I_G) of our thin SiOC films shows a decreasing trend as the C-content and process temperature increase. This observation is analogous to the trend measured for monolithic samples. The lateral crystal sizes are calculated using the Cançado correlation[66] in Equation (5) while Equations (6), (7), and (8) were used to calculate the inter-defect distances, the defect density, and the tortuosity, respectively, for the free carbon phase.[28,49,51,67,68] All values are presented in Table 2. The area under each peak is considered for all calculations taking into account all the uncertainties of the process.[67] As can be seen in Table 2, for the thin film samples, it is evident that the degree of graphitization is improved as the carbon content and temperature increase. In addition, the dispersed particles display a higher degree of graphitization than that of the matrix of the thin film with A_D/A_G equal to 1.4.

$$L_a = \left(2.4 \times 10^{-10}\right) \lambda^4 \left(\frac{A_D}{A_G}\right)^{-1}, \tag{5}$$

$$L_D^2 = 1.8 \times 10^{-9} \lambda_L^4 \frac{A_G}{A_D}, \tag{6}$$

$$n_D = \frac{2.4 \times 10^{22}}{\lambda_L^4} \frac{A_D}{A_G}, \tag{7}$$

$$L_{eq} = 77.0648 \frac{A_{2D}}{A_D}. \tag{8}$$

As shown in Figure 7, the general trend corresponds to an increase in the lateral crystal size L_a and the inter-defect distance L_D as the heat treatment temperature increases. This trend holds for both thin film and monolithic samples. Conversely, the defect density behaved inversely proportional to the heat treatment temperature with the C17-1400 thin film sample showing a high degree of steepness on its slope. Until now, there is no direct correlation found on how the defect density responds to the decreasing thickness of a material.[69–71] In comparison with the previous work of Rosenburg on the SiOC monolithic sample,[8] the calculated L_a and L_D of the SiOC film were of similar magnitude; the dispersed particles giving the largest L_a and L_D values. The L_D calculation followed the assumption that point defects are present on the phases and that the radius around the defect (r_A) where D band scattering takes place is equal to 3.1 nm.[67] Comparing the calculated L_D in this work with that of Cançado in 2011, our thin film samples obtained at 1100°C show that $L_D < r_A$, which is categorized as a highly defective region. Also in agreement with the work of Rosenburg, as the heat treatment temperature is increased, the defect density decreases (Figure 7C), and L_a and L_D increase.[10] Looking at the calculated L_{eq} of the C17-1400 samples (Figure 7D), the value calculated for the C-rich dispersed particles of the thin film is double in size as compared to that of the monolithic SiOC; while the L_{eq} of the matrix of the thin film is less than half of the value calculated for the SiOC monolith. This finding clearly indicates that the C-rich and O-depleted precipitates in the prepared SiOC-based thin films possess a significantly higher degree of graphitization than that of the matrix.

Additionally, the I_{2D}/I_G ratio of the C17-1400 sample was calculated to gain an idea of the number of graphene layers present in sample.[54,72,73] In the work of Bleu et al, a summary of I_{2D}/I_G ratio values was presented, in order to correlate the number of graphene layers in carbon-based samples.[72] The value obtained in this study which is equal to 0.144 fell under the multilayered graphene with at least 5–10 layers. In this range of graphene layers, the FWHM of the 2D peak is less reliable as it starts to appear like that of graphite. A method to confirm whether multilayered graphene or graphite exists was proposed by Roscher et al who used the coefficient of determination, namely the R^2-value, to assess the closeness of the value to the fitted regression line.[53] Multilayered graphene generates an R^2-value above the defined threshold value of 0.985 after using the Voigt profile fitting against the spectra. An R^2-value of 0.99194 is obtained for the Voigt-fitted C17-1400. This result combined with an I_{2D}/I_G ratio value of 0.144 indicates that the sp^2-hybridized carbon phase in sample C17-1400 can be described as multilayered graphene.

3.3 | Electrical conductivity of the thin film

With regard to integrating the SiOC thin film into MEMS application for further studies, it is important to investigate the electrical property of the thin SiOC films. A common way of characterizing the electrical property of a conducting or semiconducting thin film is by measuring the sheet resistance or the surface resistivity which is the lateral resistance measured across the opposite sides of a square sample.[74] In relation to other resistance measurements, the sheet resistance is independent of the size of the square allowing an easier judgment between different samples. Commonly, the four-point probe technique is preferred to measure the surface resistance as it eliminates the effect of the contact resistance and wire resistance.[75,76] In this method, the applied current comes in and out of the sample through the outer probes. The high electrical impedance of the voltmeter prevents the current from entering the inner probes, between which the voltage drop is measured. The sheet resistance measured for C11-1100 and

C17-1100 samples ranges from 765–940 kΩ/sq and 640–860 kΩ/sq, respectively. On the other hand, the sheet resistance of the C17-1400 ranges from 3.4 to 4.19 kΩ/sq.

In general, there are no explicit limits for the resistance values needed for the implementation of the material in piezoresistive thin film-based strain sensors. Different sheet resistances can be addressed by geometry changes in the design of MEMS devices. Anyway, high values (>100 kΩ/sq) result in small piezoresistors that are difficult to match to the deformation element and are strongly affected by manufacturing tolerances, reducing the overall sensitivity.[77] Furthermore, high base resistances are energy efficient but lead to noise and limit the range of measurement. In contrast, metal-like resistance values (<<1 kΩ/sq) typically require meander-like geometries to achieve sufficient base resistances. This is because low base resistances introduce large amounts of thermal energy and are therefore susceptible to thermal noise.[78] However, spatial expansion can also lead to stress average effects if it is not matched to the deforming body.[79] In addition, evaluation electronics for resistive elements in the mid-range of 0.1−5 kΩ are easier to design and available. For this reason, a resistance target range of 2−10 kΩ/sq was used in this study to perform electrical property screening of the samples. Thus, the samples prepared at 1100°C (i.e., C11-1100 and C17-1100) are considered to be not suitable for device implementation; however, C17-1400 exhibits appropriate resistance and thus high potential to be used/implemented in MEMS strain sensors.

To further characterize the electrical property and the surface quality of the sample, the topography of the film was analyzed using tunneling AFM (TUNA) and is presented in Figure 8. The roughness of the dispersed particle area (see Figure 8B), was measured to be c. 300 nm with the highest elevation at 510 nm. The average roughness of the matrix (Figure 8A) was significantly lower, that is, c. 80 nm. The roughness difference of the two phases is well-supported by the color contrast shown in Figure 4B. As mentioned above, the average thickness of the film obtained from profilometer measurement was approximately 500 nm. Using these profiles and the sheet resistance measured with the four-point probe, the conductivity of the film was calculated to be in the range of 5.27 to 8.79 S/cm. These values are two to three magnitudes larger than that of the electrical conductivities measured for monolithic samples with a similar chemical composition.[10,80–82]

Another advantage of the tunneling AFM is the simultaneous mapping of the mechanical and electrical property of sample.[83] TUNA is known to have higher current sensitivity than that of the conductive AFM mode which can measure currents down to sub-picoampere range through a highly resistive sample. In principle, the measurement depends on the tip geometry to define the lateral resolution. A bias voltage is applied between the conductive tip and the sample while scanning in contact mode generates topographic and current images.[83] With Figure 4, a representative area of 95 × 60 μm^2 was used to map out the AFM-based conductivity of the sample C17-1400 and is presented in Figure 9. A range of 0.001–2 nA was detected forming regions within the map. The current map shown in Figure 9A, which corresponds to the matrix of C17-1400, indicates that these regions are of varying sizes, and are spaced from each other by approximately 2 μm. In Figure 9B, which represents the current map of a particle in C17-1400, these regions are denser and more interconnected with each other. Some sites, depicted in dark blue color, show current values above 200 nA with the highest value recorded at 454 nA.

By comparing the electrical conductivity of C17-1100 and C17-1400, it can be concluded that the in-situ generation

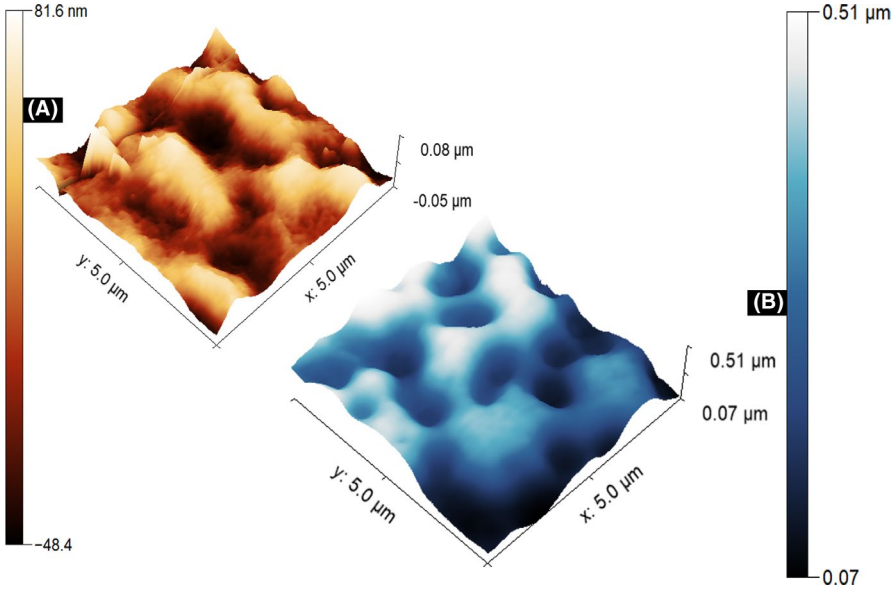

FIGURE 8 AFM Z Sensor map of C17-1400 sample. (A) The topography of the O-rich SiOC matrix with 80 nm roughness. (B) The topography of the C-rich SiOC phase with approximately 500 nm roughness. Images were taken with a 5 μm scan at a DC sample bias of 1 V

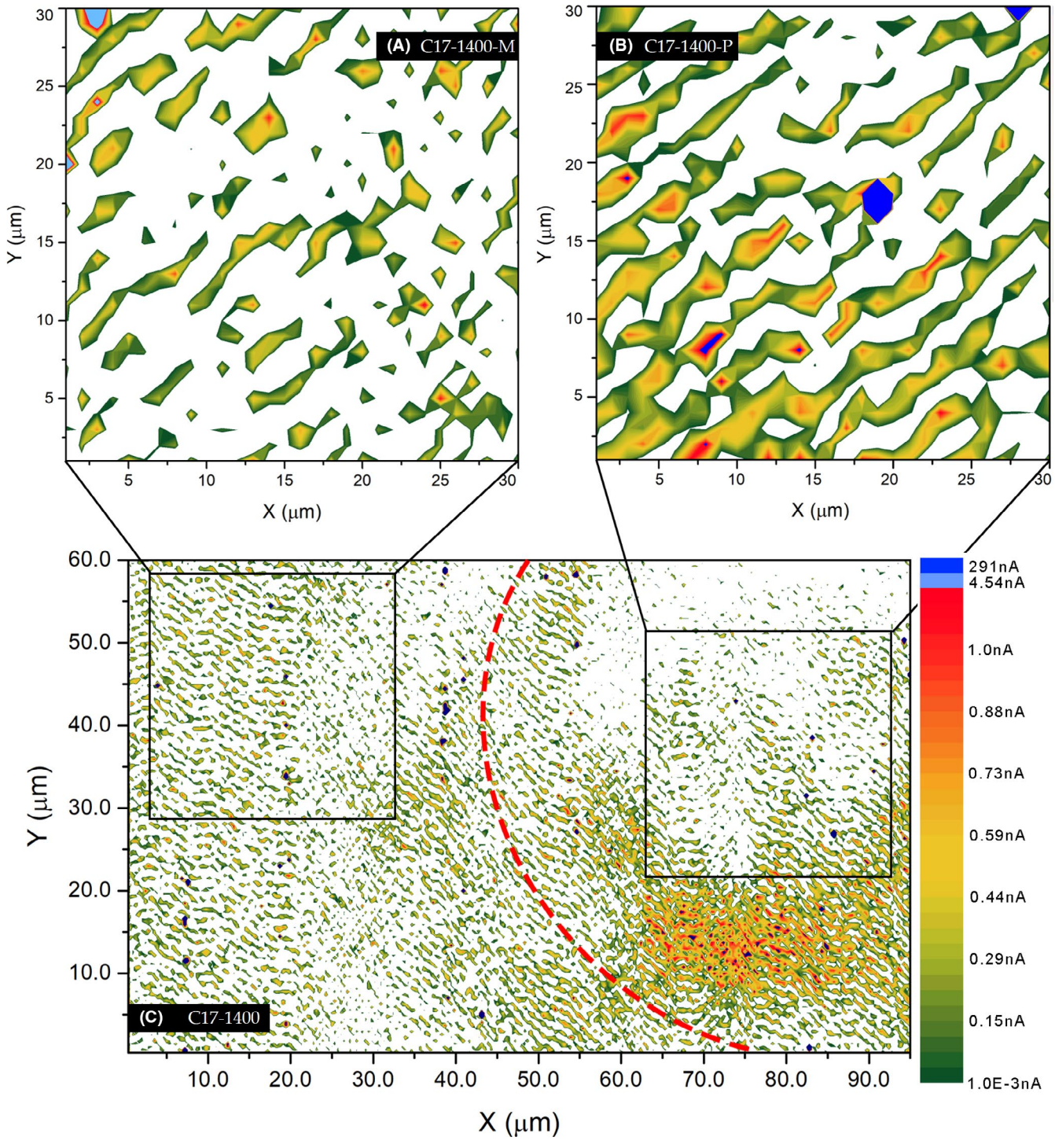

FIGURE 9 TUNA current map of the C17-1400 sample including both the matrix and a dispersed particle is shown in Image C. The red dotted line signifies the boundary of the particle from the matrix. (A) Elongated regions with current values of 0.01–2 nA were observed on the C17-1400 matrix with ~2 μm spacing between each other. (B) Elongated regions observed within the dispersed particles are denser and more interconnected as compared to those observed within the matrix. In dark blue are specific areas on the particle with current values above 100 nA with the highest recorded at 454 nA. The current map was recorded with a 5 μm scan at a DC sample bias of 1 V

of C-rich particles helps to boost the electrical conductivity of the prepared SiOC-based thin film samples (i.e., compare C17-1100 with C17-1400). This may be explained as follows: First, the C-rich particles in C17-1400 were shown to possess a higher graphitization degree of the sp^2 carbon as compared to the carbon present in the matrix of C17-1400. Consequently, the particles possess higher electrical conductivity as compared to the matrix, as supported by the TUNA

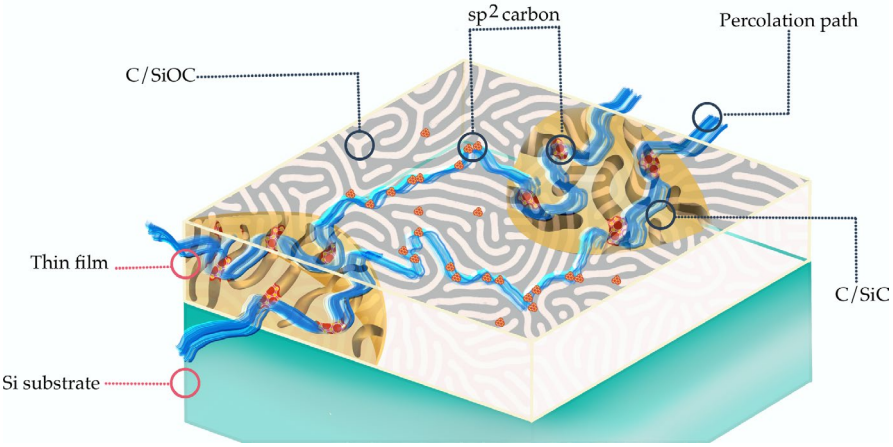

FIGURE 10 The proposed hierarchical microstructure of the prepared SiOC thin film. The yellow regions represent the large particles containing highly graphitized carbon (represented by the red hexagonal structures). The matrix also contains sp^2-hybridized carbon (small hexagonal structures) and contributes to the charge carrier transport between the large particles. The blue lines represent percolation paths throughout the sample

measurements. Even though the electrical conductivity of the particles in C17-1400 is enhanced, this is not sufficient to explain the overall increase in the electrical conductivity of C17-1400 as related to C17-1100. The volume fraction of the particles in C17-1400 was estimated to be c. 16 vol%, which is significantly lower than the percolation threshold in systems consisting of spherical conductive particles dispersed in an insulating matrix (i.e., >25 vol%[84]). This agrees with the distance between the carbon-rich particles in C17-1400, which has been estimated to be c. 2 μm. Consequently, the matrix is considered to also contribute to the electrical conductivity of C17-1400, as revealed by the TUNA measurements (Figure 9A). Thus, the electrical conduction occurs in C17-1400 through both the matrix and the dispersed particles. C17-1400 possesses a hierarchical microstructure which provides appropriate charge carrier transport: first, the carbon-enriched micro-sized particles are generated throughout the thin film upon exposure to 1400°C and exhibit enhanced electrical conductivity due to the relatively high graphitization degree of their sp^2-hybridized carbon; second, sp^2-hybridized carbon is present in the oxygen-rich matrix of C17-1400 and is responsible for the charge carrier transport between the large C-rich particles. Thus, the phase separation of sp^2-carbon, which typically occurs in polymer-derived ceramics at the nanometer scale, corroborates with the precipitation of large C-rich particles at the micro-scale and thus sustains charge carrier transport paths throughout the sample. Interestingly, the formation of the large carbon-enriched particles occurred to an extent that was sufficient to provide a large fraction of highly conductive particles in the SiOC based thin films while keeping an adequate amount of sp^2-hybridized carbon back in the matrix to sustain charge carrier transport between the large particles.

The observed microstructure in the SiOC-based thin film samples is unique and has not been observed in monolithic silicon oxycarbides. Monolithic SiOC samples were shown to provide charge carrier transport through the formation of a percolative network of sp^2-hybridized carbon via segregation at nanoscale.[85] Whereas in SiOC-based thin films, the electrical conductivity is boosted by the additional in-situ formation of large particles possessing highly graphitized carbon (see Figure 10). However, the reason for the formation of the large carbon-rich particles has not been elucidated.

4 | CONCLUSIONS

In summary, a spin coating process was designed and optimized using the Taguchi method. The initial spin speed was identified as the main factor contributing to the uniformity and homogeneity of the preceramic thin films. It was shown that the quality of the resulting ceramic thin films strongly correlates with the molecular architecture of the preceramic polymers as well as to the thermomechanical properties of the resulting SiOC composition. Thus, while a SiOC composition with a fair amount of carbon was shown to be exposed to tensile thermal stress which contributed to extensive cracking and spallation, improving the carbon content induced compressive thermal stress in the film and thus cracking and spallation were suppressed.

The prepared crack-free SiOC thin films were shown to possess a unique hierarchical microstructure consisting of large oxygen-depleted particles, mainly consisting of highly graphitized carbon and SiC, homogeneously dispersed in an oxygen-containing amorphous matrix. The matrix was shown to also contain sp^2-hybridized carbon and to contribute to charge carrier transport between the highly conductive large particles. The hierarchical microstructure of the prepared thin films has been shown to provide improved electrical conductivity as compared to

monolithic SiOC possessing the same chemical composition. Thus, the SiOC thin film prepared at 1400°C exhibits a sheet resistance of c. 2 −10 kΩ/sq and is thus considered suitable for implementation and use in miniaturized strain gauges.

CONFLICT OF INTEREST

The authors declare no conflict of interest.

AUTHOR CONTRIBUTIONS

E.R. III. and E.I. were involved in conceptualization. E.R. III and F.K. were involved in methodology, software, formal analysis, investigation, resources, data curation, and writing—original draft preparation. E.I., R.R., and H.F.S. were involved in writing—review and editing funding acquisition. E.R. III. was involved in visualization. E.I. was involved in supervision. E.R.III, F.K., and E.I. were involved in project administration. All authors have read and agreed to the published version of the manuscript.

ORCID

Emmanuel III Ricohermoso https://orcid.org/0000-0002-4093-4751
Ralf Riedel https://orcid.org/0000-0001-6888-7208
Emanuel Ionescu https://orcid.org/0000-0002-3266-3031

REFERENCES

1. Colombo P, Mera G, Riedel R, Sorarù GD. Polymer-derived ceramics: 40 years of research and innovation in advanced ceramics. J Am Ceram Soc. 2010;93(7):1805–37.
2. Riedel R, Mera G, Hauser R, Klonczynski A. Silicon-based polymer-derived ceramics: synthesis properties and applications-a review: dedicated to Prof. Dr. Fritz Aldinger on the occasion of his 65th birthday. J Ceram Soc Jpn. 2006;114(1330):425–44.
3. Ionescu E, Kleebe H-J, Riedel R. Silicon-containing polymer-derived ceramic nanocomposites (PDC-NCs): preparative approaches and properties. Chem Soc Rev. 2012;41(15):5032–52.
4. Monthioux M, Delverdier O. Thermal behavior of (organosilicon) polymer-derived ceramics. V: Main facts and trends. J Eur Ceram Soc. 1996;16(7):721–37.
5. Mera G, Navrotsky A, Sen S, Kleebe H-J, Riedel R. Polymer-derived SiCN and SiOC ceramics – structure and energetics at the nanoscale. J Mater Chem A. 2013;1(12):3826–36.
6. Bois L, Maquet J, Babonneau F, Mutin H, Bahloul D. Structural characterization of sol-gel derived oxycarbide glasses. 1. Study of the pyrolysis process. Chem Mater. 1994;6(6):796–802.
7. Schuepfer DB, Badaczewski F, Guerra-Castro JM, Hofmann DM, Heiliger C, Smarsly B, et al. Assessing the structural properties of graphitic and non-graphitic carbons by Raman spectroscopy. Carbon. 2020;1(161):359–72.
8. Rosenburg F, Ionescu E, Nicoloso N, Riedel R. High-temperature raman spectroscopy of nano-crystalline carbon in silicon oxycarbide. Materials. 2018;11(1):93.
9. Lu K, Erb D, Liu M. Thermal stability and electrical conductivity of carbon-enriched silicon oxycarbide. J Mater Chem C. 2016;4(9):1829–37.
10. Rosenburg F, Balke B, Nicoloso N, Riedel R, Ionescu E. Effect of the content and ordering of the sp2 free carbon phase on the charge carrier transport in polymer-derived silicon oxycarbides. Molecules. 2020;25(24):5919.
11. Li J, Ma PC, Chow WS, To CK, Tang BZ, Kim J-K. Correlations between percolation threshold, dispersion state, and aspect ratio of carbon nanotubes. Adv Funct Mater. 2007;17(16):3207–15.
12. Montgomery D. Design and analysis of experiments. 8th ed. Hoboken, NJ: John Wiley & Sons, Inc; 2013. 757 p.
13. Dean A, Voss D, Draguljić D. Springer Texts in Statistics: Design and Analysis of Experiments. 2nd ed., Vol. XXV. Cham: Springer International Publishing AG; 2017. p. 840.
14. Roy RK. A Primer on the Taguchi Method [Internet]. Dearborn, MI: Society of Manufacturing Engineers; 2010. [cited 2021 Jan 20]. Available from: http://search.ebscohost.com/login.aspx?direct=true&scope=site&db=nlebk&db=nlabk&AN=860349
15. Barroso G, Li Q, Bordia RK, Motz G. Polymeric and ceramic silicon-based coatings – a review. J Mater Chem A. 2019;7(5):1936–63.
16. Günthner M, Kraus T, Krenkel W, Motz G, Dierdorf A, Decker D. Particle-filled PHPS silazane-based coatings on steel. Int J Appl Ceram Technol. 2009;6(3):373–80.
17. Kraus T, Günthner M, Krenkel W, Motz G. cBN particle filled SiCN precursor coatings. Adv Appl Ceram. 2009;108(8):476–82.
18. Mandoj F, Nardis S, Di Natale C, Paolesse R. Porphyrinoid thin films for chemical sensing. In: Wandelt K, editor. Encyclopedia of Interfacial Chemistry [Internet]. Oxford: Elsevier; 2018 [cited 2020 Dec 28]. p. 422–43. Available from: http://www.sciencedirect.com/science/article/pii/B9780124095472116774
19. Makhlouf ASH. 1 - Current and advanced coating technologies for industrial applications. In: Makhlouf ASH, Tiginyanu I, editors. Nanocoatings and Ultra-Thin Films [Internet]. Woodhead Publishing; 2011 [cited 2020 Dec 28]. p. 3–23. (Woodhead Publishing Series in Metals and Surface Engineering). Available from: http://www.sciencedirect.com/science/article/pii/B9781845698126500014
20. Mukerjee R, Wu CFJ, editors. Robust parameter design. In: A Modern Theory of Factorial Designs [Internet]. New York, NY: Springer; 2006 [cited 2020 Dec 28]. p. 197–210. (Springer Series in Statistics). Available from: https://doi.org/10.1007/0-387-37344-6_9
21. Kozuka H. On ceramic thin film formation from gels: evolution of stress, cracks and radiative striations. J Ceram Soc Jpn. 2003;111(1297):624–32.
22. Kozuka H. Stress evolution on gel-to-ceramic thin film conversion. J Sol-Gel Sci Technol. 2006;40(2):287–97.
23. Kozuka H, Takenaka S, Tokita H, Hirano T, Higashi Y, Hamatani T. Stress and cracks in gel-derived ceramic coatings and thick film formation. J Sol-Gel Sci Technol. 2003;26(1):681–6.
24. Ionescu E, Linck C, Fasel C, Müller M, Kleebe H-J, Riedel R. Polymer-derived SiOC/ZrO_2 ceramic nanocomposites with excellent high-temperature stability. J Am Ceram Soc. 2010;93(1):241–50.
25. Kaspar J, Terzioglu C, Ionescu E, Graczyk-Zajac M, Hapis S, Kleebe H-J, et al. Stable SiOC/Sn nanocomposite anodes for lithium-ion batteries with outstanding cycling stability. Adv Funct Mater. 2014;24(26):4097–104.
26. Martínez-Crespiera S, Ionescu E, Schlosser M, Flittner K, Mistura G, Riedel R, et al. Fabrication of silicon oxycarbide-based microcomponents via photolithographic and soft lithography approaches. Sens Actuators Phys. 169(1):242–9.

27. Hu YY, Huang WM. Thermal stress analysis and characterization of thermomechanical properties of thin films on an elastic substrate. In: Nee A, editor. Handbook of Manufacturing Engineering and Technology [Internet]. London: Springer; 2013 [cited 2020 Dec 29]. p. 1–71. Available from: https://doi.org/10.1007/978-1-4471-4976-7_51-1
28. Stabler C, Reitz A, Stein P, Albert B, Riedel R, Ionescu E. Thermal properties of SiOC glasses and glass ceramics at elevated temperatures. Mater Basel Switz. 2018;11(2):279.
29. Rouxel T, Massouras G, Sorarù G-D. High temperature behavior of a gel-derived SiOC glass: elasticity and viscosity. J Sol-Gel Sci Technol. 1999;14(1):87–94.
30. Barber JR, editor. Plane strain and plane stress. In: Elasticity [Internet]. Dordrecht, Netherlands: Springer; 2004 [cited 2021 Jan 20]. p. 33–40. (Solid Mechanics and Its Applications). Available from: https://doi.org/10.1007/0-306-48395-5_3
31. Stoney GG, Parsons CA. The tension of metallic films deposited by electrolysis. Proc R Soc Lond Ser Contain Pap Math Phys Character. 1909;82(553):172–5.
32. Piombini H, Compoint F, Ambard C, Picart D, Belleville P, Damamme G, et al. Stress measurement of elastic sol-gel layer by photoelasticimetry - comparison with stoney. Opt Mater Express. 2016;6(2):469–85.
33. Lu K. Porous and high surface area silicon oxycarbide-based materials—a review. Mater Sci Eng R Rep. 2015;1(97):23–49.
34. Wang L, Lu K. Phase development of silicon oxycarbide nanocomposites during flash pyrolysis. J Mater Sci. 2019;54(8):6073–87.
35. Griffith WP. Raman, studies on rock-forming minerals. Part I. Orthosilicates and cyclosilicates. J Chem Soc Inorg Phys Theor. 1969;1372–7.
36. Juroszek R, Czaja M, Lisiecki R, Krüger B, Hachuła B, Galuskina I. Spectroscopic and structural investigations of blue afwillite from Ma'ale Adummim locality, Palestinian Autonomy. Spectrochim Acta A Mol Biomol Spectrosc. 2020;15(227):117688.
37. Frost RL, Čejka J, Weier ML, Martens W. Molecular structure of the uranyl silicates—a Raman spectroscopic study. J Raman Spectrosc. 2006;37(4):538–51.
38. Handke M, Urban M. IR and raman spectra of alkaline earth metals orthosilicates. J Mol Struct. 1982;1(79):353–6.
39. Chen ZY, Zhao JP, Yano T, Ooie T, Yoneda M, Sakakibara J. Observation of sp3 bonding in tetrahedral amorphous carbon using visible Raman spectroscopy. J Appl Phys. 2000;88(5):2305–8.
40. Mafra DL, Samsonidze G, Malard LM, Elias DC, Brant JC, Plentz F, et al. Determination of LA and TO phonon dispersion relations of graphene near the Dirac point by double resonance Raman scattering. Phys Rev B. 2007;76(23):233407.
41. Hodkiewicz J, Scientific TF. Characterizing carbon materials with Raman spectroscopy. 5.
42. Robertson J. Properties of diamond-like carbon. Surf Coat Technol. 1992;50(3):185–203.
43. Schwan J, Ulrich S, Batori V, Ehrhardt H, Silva SRP. Raman spectroscopy on amorphous carbon films. J Appl Phys. 1996;80(1):440–7.
44. Nemanich RJ, Glass JT, Lucovsky G, Shroder RE. Raman scattering characterization of carbon bonding in diamond and diamond-like thin films. J Vac Sci Technol A. 1988;6(3):1783–7.
45. Shroder RE, Nemanich RJ, Glass JT. Analysis of the composite structures in diamond thin films by Raman spectroscopy. Phys Rev B. 1990;41(6):3738–45.
46. Wang CZ, Ho KM. Structure, dynamics, and electronic properties of diamondlike amorphous carbon. Phys Rev Lett. 1993;71(8):1184–7.
47. Chu PK, Li L. Characterization of amorphous and nanocrystalline carbon films. Mater Chem Phys. 2006;96(2–3):253–77.
48. Roth F, Waleska P, Hess C, Ionescu E, Nicoloso N. UV Raman spectroscopy of segregated carbon in silicon oxycarbides. J Ceram Soc Jpn. 2016;124(10):1042–5.
49. Wen Q, Yu Z, Riedel R. The fate and role of in situ formed carbon in polymer-derived ceramics. Prog Mater Sci. 2020;109:100623.
50. Hodkiewicz J, Scientific TF. Characterizing carbon materials with Raman spectroscopy. 5.
51. Saini P, Sharma R, Chadha N. Determination of defect density, crystallite size and number of graphene layers in graphene analogues using X-ray diffraction and Raman spectroscopy. Indian J Pure Appl Phys IJPAP. 2017;55(9):625–9.
52. Ferrari AC, Meyer JC, Scardaci V, Casiraghi C, Lazzeri M, Mauri F, et al. Raman spectrum of graphene and graphene layers. Phys Rev Lett. 2006;97(18):187401.
53. Roscher S, Hoffmann R, Ambacher O. Determination of the graphene–graphite ratio of graphene powder by Raman 2D band symmetry analysis. Anal Methods. 2019;11(9):1224–8.
54. Ferrari AC. Raman spectroscopy of graphene and graphite: Disorder, electron–phonon coupling, doping and nonadiabatic effects. Solid State Commun. 2007;143(1):47–57.
55. Zólyomi V, Koltai J, Kürti J. Resonance Raman spectroscopy of graphite and graphene. Phys Status Solidi B. 2011;248(11):2435–44.
56. Lindsay L, Broido DA. Optimized Tersoff and Brenner empirical potential parameters for lattice dynamics and phonon thermal transport in carbon nanotubes and graphene. Phys Rev B. 2010;81(20):205441.
57. Koukaras EN, Kalosakas G, Galiotis C, Papagelis K. Phonon properties of graphene derived from molecular dynamics simulations. Sci Rep. 2015;5(1):12923.
58. Roth F, Schmerbauch C, Ionescu E, Nicoloso N, Guillon O, Riedel R. High-temperature piezoresistive C/SiOC sensors. J Sens Sens Syst. 2015;4(1):133–6.
59. Bokobza L, Bruneel J-L, Couzi M. Raman spectra of carbon-based materials (from graphite to carbon black) and of some silicone composites. C. 2015;1(1):77–94.
60. Das A, Chakraborty B, Sood AK. Raman spectroscopy of graphene on different substrates and influence of defects. Bull Mater Sci. 2008;31(3):579–84.
61. Calizo I, Ghosh S, Bao W, Miao F, Ning Lau C, Balandin AA. Raman nanometrology of graphene: temperature and substrate effects. Solid State Commun. 2009;149(27):1132–5.
62. Calizo I, Bao W, Miao F, Lau CN, Balandin AA. The effect of substrates on the Raman spectrum of graphene: Graphene- on-sapphire and graphene-on-glass. Appl Phys Lett. 2007;91(20):201904.
63. Kaniyoor A, Ramaprabhu S. A Raman spectroscopic investigation of graphite oxide derived graphene. AIP Adv. 2012;2(3):032183.
64. King AAK, Davies BR, Noorbehesht N, Newman P, Church TL, Harris AT, et al. A new Raman metric for the characterisation of graphene oxide and its derivatives. Sci Rep. 2016;6(1):19491.
65. Merkulov VI, Lannin JS, Munro CH, Asher SA, Veerasamy VS, Milne WI. UV studies of tetrahedral bonding in diamondlike amorphous carbon. Phys Rev Lett. 1997;78(25):4869–72.
66. Cançado LG, Takai K, Enoki T, Endo M, Kim YA, Mizusaki H, et al. General equation for the determination of the crystallite

size La of nanographite by Raman spectroscopy. Appl Phys Lett. 2006;88(16):163106.
67. Cançado LG, Jorio A, Ferreira EHM, Stavale F, Achete CA, Capaz RB, et al. Quantifying defects in graphene via Raman spectroscopy at different excitation energies. Nano Lett. 2011;11(8):3190–6.
68. Larouche N, Stansfield BL. Classifying nanostructured carbons using graphitic indices derived from Raman spectra. Carbon. 2010;48(3):620–9.
69. Wang Y, Liu H, Shen W. A convenient and effective method to deposit low-defect-density nc-Si:H thin film by PECVD. Nanoscale Res Lett. 2018;13(1):234.
70. La Via F, Severino A, Anzalone R, Bongiorno C, Litrico G, Mauceri M, et al. From thin film to bulk 3C-SiC growth: understanding the mechanism of defects reduction. Mater Sci Semicond Process. 2018;1(78):57–68.
71. Takami A, Arimoto S, Naomoto H, Hamamoto S, Ishihara T, Kumabe H, et al. Thickness dependence of defect density in thin film silicon formed on insulator polycrystalline by zone-melting recrystallization [solar cells]. In: Proceedings of 1994 IEEE 1st World Conference on Photovoltaic Energy Conversion - WCPEC (A Joint Conference of PVSC, PVSEC and PSEC). Vol. 2. 1994. p. 1394–7. Available from: https://doi.org/10.1109/WCPEC.1994.520208
72. Bleu Y, Bourquard F, Loir A-S, Barnier V, Garrelie F, Donnet C. Raman study of the substrate influence on graphene synthesis using a solid carbon source via rapid thermal annealing. J Raman Spectrosc. 2019;50:1630–41.
73. Gayathri S, Jayabal P, Kottaisamy M, Ramakrishnan V. Synthesis of few layer graphene by direct exfoliation of graphite and a Raman spectroscopic study. AIP Adv. 2014;4(2):027116.
74. Ghorbani MM, Taherian R. 12 - Methods of Measuring Electrical Properties of Material**Hereby from Keithley Co. and Dr. Michael B. Heaney is appreciated due to valuable content used in this chapter. In: Taherian R, Kausar A, editors. Electrical Conductivity in Polymer-Based Composites [Internet]. William Andrew Publishing; 2019 [cited 2021 Jan 26]. p. 365–94. (Plastics Design Library). Available from: http://www.sciencedirect.com/science/article/pii/B9780128125410000124
75. Chung DDL. A critical review of piezoresistivity and its application in electrical-resistance-based strain sensing. J Mater Sci. 2020;55(32):15367–96.
76. Smits FM. Measurement of sheet resistivities with the four-point probe. Bell Syst Tech J. 1958;37(3):711–8.
77. Kumar SS, Pant BD. Design principles and considerations for the 'ideal' silicon piezoresistive pressure sensor: a focused review. Microsyst Technol. 2014;20(7):1213–47.
78. Lotichius J. Modellbildung der Messunsicherheit resistiver Sensorsysteme [Internet] [Ph.D. Thesis]. [Darmstadt]: Technische Universität Darmstadt. 2017. Available from: http://tuprints.ulb.tu-darmstadt.de/6845
79. Clark SK, Wise KD. Pressure sensitivity in anisotropically etched thin-diaphragm pressure sensors. IEEE Trans Electron Devices. 1979;26(12):1887–96.
80. Cordelair J, Greil P. Electrical conductivity measurements as a microprobe for structure transitions in polysiloxane derived Si–O–C ceramics. J Eur Ceram Soc. 2000;20(12):1947–57.
81. Nguyen VL, Zanella C, Bettotti P, Sorarù GD. Electrical conductivity of SiOCN ceramics by the powder-solution-composite technique. J Am Ceram Soc. 2014;97(8):2525–30.
82. Terauds K, Sanchez-Jimenez PE, Raj R, Vakifahmetoglu C, Colombo P. Giant piezoresistivity of polymer-derived ceramics at high temperatures. J Eur Ceram Soc. 2010;30(11):2203–7.
83. Li C, Minne S, Pittenger B, Mednick A. Simultaneous Electrical and Mechanical Property Mapping at the Nanoscale with PeakForce TUNA. Santa Barbara, CA: Bruker Corporation; 2011. p. 12 (Application Note 132).
84. Rahaman M, Aldalbahi A, Govindasami P, Khanam N, Bhandari S, Feng P, et al. A new insight in determining the percolation threshold of electrical conductivity for extrinsically conducting polymer composites through different sigmoidal models. Polymers. 2017;9(10):527.
85. Toma L, Kleebe H-J, Müller MM, Janssen E, Riedel R, Melz T, et al. Correlation between intrinsic microstructure and piezoresistivity in a SiOC polymer-derived ceramic. J Am Ceram Soc. 2012;95(3):1056–61.

SUPPORTING INFORMATION

Additional supporting information may be found online in the Supporting Information section.

How to cite this article: Ricohermoso EI, Klug F, Schlaak H, Riedel R, Ionescu E. Electrically conductive silicon oxycarbide thin films prepared from preceramic polymers. *Int J Appl Ceram Technol*. 2022;19:149–164. https://doi.org/10.1111/ijac.13800